Supporting Information

A new paradigm to assess brain cell morphology by diffusion-weighted MR spectroscopy *in vivo*

Authors: Marco Palombo[1,2], Clémence Ligneul[1,2], Chloé Najac[1,2], Juliette Le Douce[1,2], Julien Flament[1,3], Carole Escartin[1,2], Philippe Hantraye[1,2,3], Emmanuel Brouillet[1,2], Gilles Bonvento[1,2], Julien Valette[1,2*]

Affiliations:

[1] Commissariat à l'Energie Atomique et aux Energies Alternatives (CEA), Direction de la Recherche Fondamentale (DRF), Institut d'Imagerie Biomédicale (I2BM), MIRCen, F-92260 Fontenay-aux-Roses, France

[2] Centre National de la Recherche Scientifique (CNRS), Université Paris-Sud, Université Paris-Saclay, UMR 9199, Neurodegenerative Diseases Laboratory, F-92260 Fontenay-aux-Roses, France

[3] Institut National de la Santé et de le Recherche Médicale (INSERM), Unité Mixte de Service UMS 27, F-92260 Fontenay-aux-Roses, France

***Corresponding authors**: Dr. Marco Palombo, Commissariat à l'Energie Atomique et aux Energies Alternatives (CEA), Direction de la Recherche Fondamentale (DRF), Institut d'Imagerie Biomédicale (I2BM), MIRCen, 8 Route du Panorama, 92260 Fontenay-aux-Roses, France, Tel. +33 1 46 54 92 96, e-mail: marco.palombo@cea.fr and Dr. Julien Valette, Commissariat à l'Energie Atomique et aux Energies Alternatives (CEA), Direction de la Recherche Fondamentale (DRF), Institut d'Imagerie Biomédicale (I2BM), MIRCen, 8 Route du Panorama, 92260 Fontenay-aux-Roses, France, Tel. +33 1 46 54 81 30, e-mail: julien.valette@cea.fr

SI Text

The outline of Supporting Information (SI) is as follows: section I) provides some details about diffusion-weighted MRS acquisition and processing; in section II), the process of synthetic cell generation is described; section III) describes in details how the ADC is computed in a set of synthetic cells; in section IV) the influence of the morphometric statistics on metabolite ADC is studied by using the numerical simulation approach described in the Materials and Methods; in section V) the stability of estimated parameters relative to noise is assessed, by performing extensive Monte Carlo based on ground truth morphology; section VI) reports how standard deviation and statistical significance were calculated for estimated parameters based again on a Monte Carlo procedure; section VII) provides details about the effect of long axons on measured ADC; and section VIII) gives further information regarding the generation of the synthetic tissue used for comparison with histology.

I) Diffusion-weighted MRS acquisition and processing

Primate experiments were performed on healthy male macaque monkeys (*Macaca fascicularis*, body weight 4-6 kg) anesthetized with propofol, using a 7 T MRI scanner (Agilent, USA) equipped with a 29-cm (inner diameter) gradient coil reaching 100 mT/m along each axis. The animals were held in the sphinx position and the head was positioned in a stereotaxic frame with a bite-bar and ear rods, and maintained at 37°C by warm air. A ^{1}H quadrature surface coil was used for radiofrequency emission and reception. An 18×18×18 mm^{3} (5.8 mL) voxel was positioned in the region of interest. The methodology used is exactly the same as described in our recent work in the primate brain (20), i.e. spectra were acquired with a diffusion contrast Δb=3000 s/mm² using a STEAM (Stimulated Echo Acquisition Mode) sequence modified for diffusion-weighting, and t_d was changed by changing the mixing time.

The methodology used in the monkey brain is exactly the same as described in our recent work in the primate brain (20), and actually metabolite ADC at t_d=86, 361, 511, 661and 1011 ms used in the present work have already been presented in this latter article. Here we acquired an additional point at t_d=2011 ms on five animals, using the same method. Briefly, a ^{1}H quadrature surface coil was used for radiofrequency emission and reception. An 18×18×18 mm^{3} (5.8 mL)

voxel was positioned in the region of interest. Spectra were acquired with a diffusion contrast Δb=3000 s/mm² using a STEAM (Stimulated Echo Acquisition Mode) sequence modified for diffusion-weighting by inserting one diffusion gradient pulse (duration δ=5 ms) during each half of the echo (the echo time TE being 18 ms). In the range of *b*-values used in the present work, the logarithm of signal attenuation can be considered linear for metabolites, therefore only the diffusion contrast Δb=3000 s/mm² is relevant, irrespective of the diffusion-weighting induced by selection gradients only (from 18 s/mm² at t_d=86 ms to 480 s/mm² at t_d=2011 ms). Hence for simplicity we will write "b=0" at all t_d when no diffusion gradients are applied. The cross-terms between diffusion gradients and selection gradients must of course be considered to get a diffusion contrast Δb exactly equal to 3000 s/mm². Here acquisitions were done with positive and negative diffusion gradient polarities to cancel for these cross-terms by taking the geometric mean of the signal (see ref. (20) for details). While individual scan phasing was performed in our previous monkey study for $t_d \leq$1011 ms to correct for translational motion artifact, here metabolite signal on single scans at t_d=2011 ms was too low (due to T_1 relaxation during the mixing time) for such rephasing to be performed. However, as discussed below, the absence of individual scan phasing has negligible effect at ultra-long t_d. Experimental macromolecule signal (acquired by metabolite nulling) was acquired to remove macromolecule contribution from metabolite signal. Metabolite signal was quantified using LCModel (34), and signal quantification was estimated reliable (Cramer-Rao lower bounds <5%) for total NAA (NAA), total creatine (tCr), total choline (tCho), glutamate (Glu) and myo-inositol (Ins). The ADC was finally calculated as the logarithm of signal attenuation divided by *b*.

Rodent experiments were performed on healthy C57/BL6 male mice (body weight ~30 g) anesthetized at low isoflurane dose (<1.5%), using an 11.7 T MRI scanner (Bruker BioSpec, Germany) equipped with a 9-cm (inner diameter) gradient coil reaching 752 mT/m along each axis. The animals were positioned in a stereotaxic frame with a bite-bar and ear rods, and maintained at 37°C by circulation of warm water. Radiofrequency transmission and reception was achieved using a quadrature surface cryoprobe, and acquisitions were performed in a 5×2.4×6 mm^3 (72 µL) voxel. A DW-MRS approach comparable to that described above for the monkey was used, except that only a single gradient polarity was used and the *b* value was calculated exactly taking all sequence gradients into account (so that acquisitions with both diffusion gradient polarities was unnecessary). TE was 30 ms and δ was 2 ms. The diffusion

contrast was also exactly set to Δb=3000 s/mm² (here again, the contribution of selection gradients alone was small, so we will just write "b=0" and "b=3000 s/mm²"). Spectra were acquired for t_d=52, 352, 502, 652, 1002 and 2002 ms. An array of spectra with and without diffusion weighting for all t_d is presented in Fig. S1. Post-processing was similar to the monkey data, including individual scan phasing except at t_d=2002 ms. Signal quantification was estimated reliable (Cramer-Rao lower bounds <5%) for NAA, tCr, tCho, Glu, Ins and also for taurine (Tau). Sometimes the scanning sessions had to be stopped before all t_d were acquired for a given animal, and in the end the number of measurements was N=8 for t_d=52, 352 and 502 ms, N=5 for t_d =652 and 1002 ms, and N=7 for t_d=2002 ms.

The standard deviation of the phase, s.d.(ϕ), as calculated on an array of individual scans, is given by s.d.(ϕ) = $\gamma\delta G_{diff}$ × s.d.(x), where γ is the gyromagnetic ratio, δ the diffusion gradient duration, G_{diff} the diffusion gradient amplitude, and s.d.(x) the standard deviation of sample's bulk translation along the gradient direction during t_d. If individual scans are summed without phase correction, incoherent averaging may result in artifactual signal loss, resulting in overestimated ADC. However, when t_d is increased while b is kept constant, G_{diff} is decreased as the inverse of the square root of t_d. Meanwhile, s.d.(x) cannot increase beyond a certain threshold (imposed by the mechanical limits of the system). Thus, in the limit of ultra-long t_d, s.d.(ϕ) is expected to decrease as the as inverse of the square root of t_d, so that artifactual signal loss due to incoherent average in the absence of individual scan phasing will become insignificant. We experimentally verified at each scanning session that, at t_d=2 seconds and b=3000 s/mm², s.d.(ϕ) on the water peak (calculated over 64 scans without water suppression) was always smaller than 10° (*versus* up to 20-25° at the shortest t_d), corresponding to ~1.5-2% artifactual signal loss in the worst case as measured on the sum of the scans. In this context, ADC at the longest t_d is overestimated at most by ~0.005 µm²/ms, which is smaller than the standard error of the mean.

II) Synthetic cell generation

We propose to treat as a graph the numerous processes radiating from the cell body and exhibiting successive ramifications, and we consider three morphometric statistics, each described by two parameters (mean and s.d.), to characterize the graph topology, as illustrated in Fig. 1A of the main document: the process number ($N_{proc} \pm SD_{Nproc}$); the segment length ($L_{segment}$

± $SD_{Lsegment}$); and the branching number (N_{branch} ± $SD_{Nbranch}$). Each node of the graph will correspond to a branching point between segments of a process, or to a segment's end, and will be associated with coordinates in the 3D space. Each arc between two different nodes will correspond to the segment of a process, and will be associated with the two nodes $\{i,j\}$ that the segment is connecting. We equip each arc (of length L_{ij}) with a 1D spatial coordinate system: the initial coordinate 0 corresponding to the node indexed with the smallest integer ($\min(i,j)$), and L_{ij} corresponding to the node indexed with the biggest integer ($\max(i,j)$), so that each point in the arc can be referenced by a single coordinate x, with $0<x<L_{ij}$. At any time, the position of a given particle, defined by its 1D position along a given arc, can be converted to 3D spatial positions, which is necessary for example to compute the phase evolution under the presence of gradients.

The graph is built iteratively, node after node starting from the cell body (node 1), by adding new arcs that are drawn randomly according to the morphometric statistics. First, the number of cellular processes radiating from the cell body is drawn according to the process number statistics. Then, for each process, the length of the first arc (i.e. the length of the process between the cell body and the first branching point) is drawn according to the segment length statistics, leading to the creation of a new node at the extremity of this new segment. It is then determined, according to the branching number statistics, whether the process stops at this new node, or if this new node is actually a branching point where the process divides into two new arcs, which will then be drawn according to the "segment length" statistics. The last two steps are repeated on each new arc, until it reaches an end (i.e. a draw according to the "branching number" statistics imposes that there is no new division beyond the current node). This process of synthetic cell generation can be repeated for many cells, in order to obtain a good sampling of the morphometric statistics used. Examples of different cells following the same statistics are shown in Fig. 1B of the main document.

III) Simulating metabolite ADC by Monte Carlo simulations in synthetic cells

At the beginning of the simulation, N=2000 particles are positioned randomly inside all arcs of the cell-graph. Then, for each particle and each time-step τ (τ= 0.5 ms), a displacement of magnitude $\sqrt{2D_{intra}\tau}$ is randomly drawn towards smaller or greater x values. If its displacement brings the particle through a node connected to other arcs, the particle is randomly assigned a

new arc connecting this node (but different from the arc it comes from) and assigned a coordinate in this new arc so that the total displacement during the time step is equal to $\sqrt{2D_{intra}\tau}$. If its displacement brings the particle through a node connected to no other arc, i.e. the current arc is at the extremity of a cellular process, then the particle undergoes a simple reflection at the extremity, so that the total displacement during the time step is equal to $\sqrt{2D_{intra}\tau}$. The corresponding diffusion-weighted signals arising from each cell were computed by using the phase accumulation approach (29) and then summed over the whole set of cell-graphs to obtain the coarse-grained averaged ADC, comparable with experimental one.

Specifically, at each update (corresponding to time *t*), the *j*-th spin diffusing within the *k*-th cell-graph undergoes a phase variation $d\phi_j(t)$:

$$d\phi_j(t) = \gamma \vec{g}(t) \cdot \vec{r}_j(t)\tau \qquad (1)$$

where $\vec{g}(t)$ is the diffusion sensitizing gradient vector, assumed constant over the time-step, and $\vec{r}_j(t)$ the *j*-th spin's position (in 3D) at time t, τ is the duration of the time-step, and γ is the gyromagnetic ratio for the specific nuclear species investigated (hydrogen nuclei in our case). The synthetic signal for the cell-graph *k* is generated by summing the contributions from all spins at the end of the sequence (at time t_{seq}):

$$S_k = \sum_j e^{i\phi_j} \qquad (2)$$

where $\phi_j = \sum_{t=0}^{t_{seq}} d\phi_j(t)$. The total signal *S*, corresponding to the whole synthetic tissue, is the sum of the signal arising from particles diffusion in each of the 80 cell-graphs generated for each set of parameter values, weighted by the "volume" V_k of the cell-graph to correct for the fact that the same number of particles (*N*=2000) was assigned to each cell-graph (in our implementation, V_k is the sum of the lengths of all the segments in cell-graph *k*):

$$S = \sum_k V_k |S_k| \qquad (3)$$

Finally, it is straightforward to compute the *ADC* as:

$$ADC = -\frac{\ln(S/S_0)}{b} \qquad (4)$$

where S_0 is the signal obtained without any diffusion sensitizing gradients (i.e. with $\vec{g} = 0$) and *b* is the so called diffusion-weighting factor defined as:

$$b = \gamma^2 \int_0^{t_{seq}} dt \, [\int_0^t \vec{g}(t')\, dt']^2 \qquad (5)$$

Note that in this work ADC was measured/simulated using only two *b*-values. Although in this low *b*-value range metabolite attenuation is essentially mono-exponential, our simulation programs can account for the actual *b*-values, which might be critical if higher *b* were used. In particular, the deviations from mono-exponentiality that arise from restricted diffusion of a single metabolite pool within thin cylinders as assumed in our model, which yields a non-mono-exponential attenuation, is a feature that emerges from our model when higher *b*-values are simulated.

IV) Influence of the morphometric statistics on metabolite ADC

The rationale for going at long t_d is to be sensitive to long-range geometry, in particular restriction at the extremity of cell processes. One may wonder if long t_d DW-MRS is only sensitive to restriction at the extremity of processes, i.e. only depends on the total process length $L_{segment} \times N_{branch}$, or if it can allow untangling the effect of $L_{segment}$ and N_{branch}. To test that, we simulated diffusion in different sets of cells all satisfying $L_{segment} \times N_{branch}$=100 µm but varying mean $L_{segment}$ or N_{branch}. It appears that ADC time dependency does not only depend on total process length, but specifically depends on $L_{segment}$ and N_{branch}: large ($N_{branch}/L_{segment}$) ratio leads to strong ADC drop before stabilization at longer t_d, while small ($N_{branch}/L_{segment}$) ratio leads to steadier ADC decrease as t_d is increased (Fig. S2A). D_{intra} was set to 0.5 µm²/ms (22) in all these simulations.

It is also possible to test how mean and s.d. of segment length $L_{segment}$ affect the intracellular ADC as a function of t_d. While mean $L_{segment}$ has a strong effect (shorter $L_{segment}$ leading to stronger ADC drop), the s.d. has a significant impact at long diffusion times only (Fig. S2B), suggesting that cellular heterogeneity should not be accessible by conventional diffusion measurements typically performed for t_d shorter than 100-200 ms. Conversely, thanks to the ultra-long t_d acquisition reported here, it is possible to estimate the degree of heterogeneity in cellular morphology and extract the corresponding statistics, characterizing the brain tissue. The

same effect is observed for N_{branch} (not reported). In contrast, the process number has no effect on the ADC (Fig. S2C).

V) Stability of estimated parameters relative to experimental noise

Stability of the estimated parameters with respect to experimental noise was evaluated using a Monte Carlo approach (250 draws of noised datasets). A reference dataset (ADC values as a function of t_d for t_d=52, 352, 502, 652, 1002 and 2002 ms) was simulated with the following "ground truth" parameters values: D_{intra}=0.45 μm^2/ms; N_{branch}=3; $L_{segment}$=40 μm; $SD_{Nbranch}$=3; $SD_{Lsegment}$=10 μm. At each Monte Carlo iteration, random Gaussian noise was generated with s.d. comparable to experimental s.d. on ADC (~15%) and added to the reference dataset to generate a new dataset, which was analyzed using the fitting pipeline. Fitting results are summarized and reported in Fig. S3.

Stability of the fitting pipeline with respect to experimental noise was quantitatively evaluated by investigating the accuracy (a measure of the proximity of estimated results to the true values) and the precision (the reproducibility of the estimation) by studying the bias and the coefficient of variation (CV) of the estimated parameters (reported in Table S2), defined as:

$$Bias = \frac{\mu}{\mu_{true}} - 1$$

$$CV = \frac{\sigma}{\mu_{true}}$$

where μ_{true} and μ are the "true" and the estimated mean value of each fitting parameter, respectively, and σ is the s.d. of the estimated fitting parameter. The μ and σ parameters were obtained by fitting a Gaussian distribution to the distribution of estimated fitting parameters reported in Fig. S3. The analysis of fitting stability (Table S2) shows that the fitting pipeline is overall very robust to experimental noise fluctuation.

VI) Determination of parameters' standard deviations and statistical significances

Morphological parameters were determined from the fit of average data. Hence, we had to use a Monte Carlo procedure to estimate the standard deviation for these parameters. For each metabolite, 50 noised datasets were generated from the best fit of average experimental data, with noise variance corresponding to the variance between best fit and data, and analyzed using the simulation-fitting pipeline. At the end of this procedure, we obtained a distribution of 50 values for each parameter and each metabolite, from which the s.d. can be calculated. These s.d. are reported in brackets in Table 1.

To determine whether the differences between metabolites or species are significant or not, statistical analysis must be done on the distributions generated by the Monte Carlo procedure described just above. To provide statistical analysis for a given parameter when comparing two conditions (e.g. comparison between metabolites, or between species), we propose to perform a standard permutation test, as briefly summarized here:

- The difference in means D between the estimated parameters for the two conditions is calculated.
- The Monte Carlo distributions of parameter values under the two conditions are pooled, and the difference in sample means d is calculated and recorded for every possible way of dividing these pooled values into two groups of the same size of the original groups (here taken equal to 6) on which the mean was calculated.
- The p-value of the two-tailed test is calculated as the proportion of sampled permutations where $\text{abs}(d) \geq \text{abs}(D)$.

To correct for multiple comparisons, we must consider the total number of comparisons performed: within each species, 5 metabolites are compared for each of the 4 morphological parameters, representing a total of $4\times(5\times4)/2=40$ comparisons for each species. In addition, the interspecies comparisons are performed for the 5 metabolites and the 4 morphological parameters, i.e. 20 comparisons. This makes a total of 100 comparisons. Hence, considering a very conservative Bonferroni correction, the standard threshold for statistical significance must be reduced from $p=0.05$ to $p=5\times10^{-4}$. All p-values are reported in Table S3 for inter-metabolites comparisons within the mouse brain, in Table S4 for inter-metabolites comparisons within the monkey brain, and in Table S5 for interspecies comparisons.

To illustrate the dispersion of the fits of all noised dataset obtained during the Monte Carlo procedure, as well as to visually convince the reader that metabolites can be discriminated

according to their diffusion behavior despite experimental scatter, we provide some figures presenting various relevant comparisons between metabolites in the mouse brain (Fig. S4), in the monkey brain (Fig. S5), and between species (Fig. S6). In these figures, the diffusion curves were normalized relative to the experimental ADC at the shortest t_d to facilitate visual comparison. The envelope of the fits was generated by taking the most extreme fits obtained during the Monte Carlo procedure.

VII) Effect of long axons on intracellular ADC

An important aspect to consider is the potential presence of very long axons within the investigated volumes of interest (VOI), which can actually represent a large volume fraction of the VOI, e.g. when the latter contains a significant amount of white matter. Furthermore, the average volume fraction of white matter is expected to be much lower within the VOI in the mouse compared to the macaque brain, which might bias the interspecies comparison. In order to test how different volume fractions of long axons affect the time-dependence of intracellular ADC, we performed simulations considering different values of long axons volume fractions, f_{axon}, ranging from 0% to 50% of the total cellular volume. A synthetic tissue composed of N_{cell} = 2500 cell-graphs was generated according to the following morphometric statistics: N_{proc} = 10 ± 5; N_{branch} = 4 ± 2 and $L_{segment}$ = (30 ± 10) μm. According to each f_{axon} value, N_{axon} cell-graphs among the N_{cell} were added a single long process of 1 mm length so that the cumulated length of the N_{axon} long fibers corresponds to a fraction f_{axon} of the sum of the length of all the segments (i.e. the total "cell volume"). Metabolite diffusion was simulated in the N_{cell} cell-graphs, assuming D_{intra}=0.50 μm^2/ms. The simulation-fitting pipeline was then used to extract the estimated D_{intra} and the morphometric statistics of this synthetic tissue, without any *a priori* constraint on cell morphology (i.e. using cell-graphs that *do not* exhibit very long axons, similar to the cell-graphs used to fit experimental ADC).

Results reported in Fig. S7 show that different long axons volume fractions only bias the estimated D_{intra}. While the estimated D_{intra} is significantly (two-tailed p<0.001 from unpaired t-test) higher than the actual value for $f_{axon}\geq$20%, the four estimated morphometric parameters are consistent with the actual ones, whatever the f_{axon} values (Fig. S7). An intuitive explanation for this result is that the presence of rare, very long processes does not significantly affects the

distribution of morphometric parameters, which is dominated by the numerous processes of the dendritic tree.

Interestingly, this is very consistent with the results reported in Table 1 of the main text, concerning metabolites D_{intra} values estimated from the mouse and macaque data. It is known that, in the macaque brain, a larger volume is occupied by white matter than in mouse brain. Actually, even astrocytes exhibit some rare, long processes in the primate (27,28). Consistently with the presence to a higher degree of some long astrocytic processes and axons in the macaque, estimated D_{intra} are lower in the mouse brain.

VIII) Synthetic tissue generation and comparison with real histological slice

Here we consider Ins and tCho compartments in order to obtain a synthetic tissue representative of astrocytes, and directly comparable with tissues stained for glial fibrillary acidic protein (GFAP) observed by confocal microscopy. For each metabolite's compartment, 1200 cell-graphs were generated according to the morphometric statistics for Ins and tCho compartments reported in Table 1 of the main text, for both mouse and macaque. Cell-graph cores were placed on a three-dimensional randomized face-centered cubic lattice with random step uniformly distributed between 0 μm and 25 μm, a lattice step of 50 μm and total lattice dimension (2400×2400×600) μm, avoiding any cell-graph overlap (Fig. S8). A slice with the same thickness as the histological section (40 μm) was cut from the synthetic tissue and a realistic image of the slice was rendered by using a ray-tracing algorithm implemented on POV-Ray (http://www.povray.org/). The resulting images were rescaled in order to match the same resolution as the histological ones, and reported in Fig. 3 of the main text. In order to achieve a higher degree of realism, each segment of the cell-graphs was rendered as a rough-surfaced cylinder, whose diameter was directly taken from histological data (27,28). Specifically, a diameter of (2.5 ± 0.5) μm was used for the first segments, i.e. the segments radiating from the soma. Then, at each bifurcation, the diameter of the successive segments was reduced by a factor 1/3.

The bi-dimensional image representing the synthetic slice was then binarized and used to perform Sholl-based analysis on the synthetically reproduced tissue. An example of this

procedure, and relative results, are shown in Fig. S9, where a comparison with Sholl-based analysis of real histological images is also reported.

Figure S1: Typical diffusion spectra acquired in the mouse brain at low ("*b*=0 s/mm²") and high ("*b*=3000 s/mm²") diffusion-weighting, for all measured diffusion times t_d. To facilitate visual comparison, spectra were rescaled so that the height of the NAA peak is identical at *b*=0 for all t_d. Note the very good stability of slow-diffusion macromolecule signal at 0.9 ppm, demonstrating the absence of artefactual attenuation at *b*=3000 s/mm².

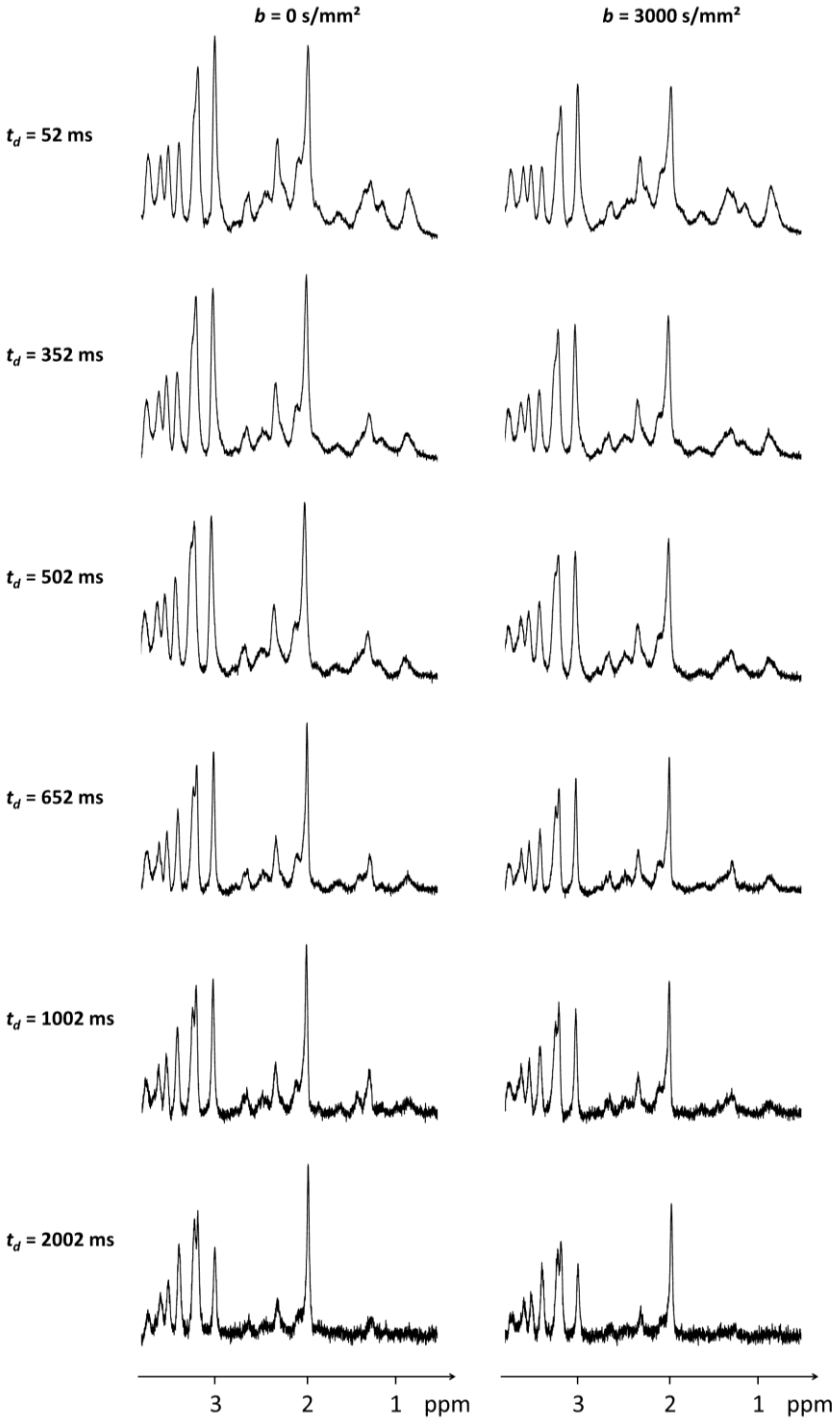

Figure S2: Influence of the morphometric statistics on the observed ADC. (A) Concomitant effects of different N_{branch} and $L_{segment}$ values on the observed ADC, keeping constant $L_{segment} \times N_{branch}$=100 µm (and taking here $SD_{Lsegment}$ and $SD_{Nbranch}$=0). (B) Effect of the mean and standard deviation of $L_{segment}$ on the observed ADC. The black curves correspond to the indicated $L_{segment}$ with $SD_{Lsegment}$=0, the grey curves for indicated $L_{segment}$ with $SD_{Lsegment}$=0.5×$L_{segment}$. (C) Effect of different values of N_{proc} on the observed ADC (taking here SD_{Nproc}=0).

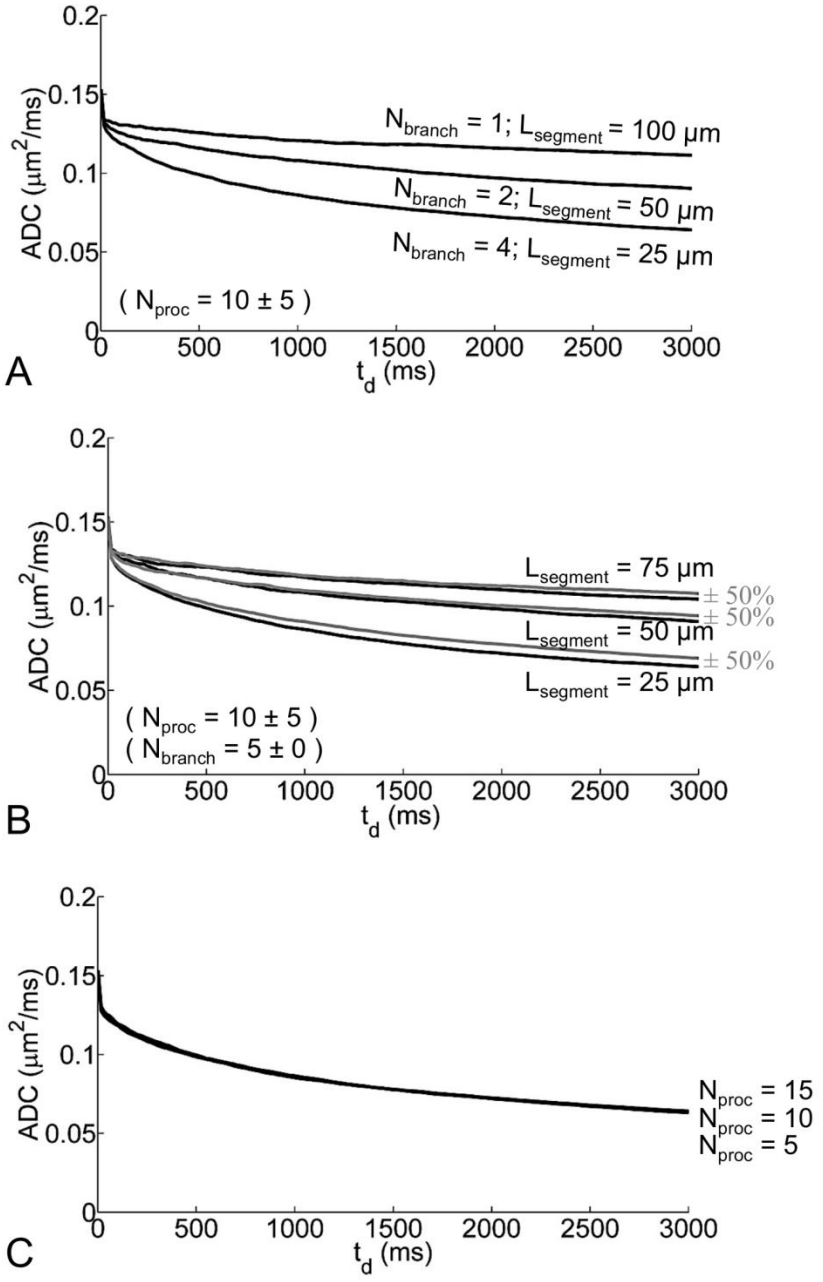

Figure S3: **Accuracy and precision of the simulation fitting pipeline.** Frequency histograms for the parameters estimated from independent fits of 250 artificially noised datasets. Dataset was created as described in this appendix (*Section V*). The red curve represents the best Gaussian distribution fitting the data, and the corresponding mean (μ) and s.d. (σ) are reported in the inset. The black arrows indicate the true value for each fitting parameter.

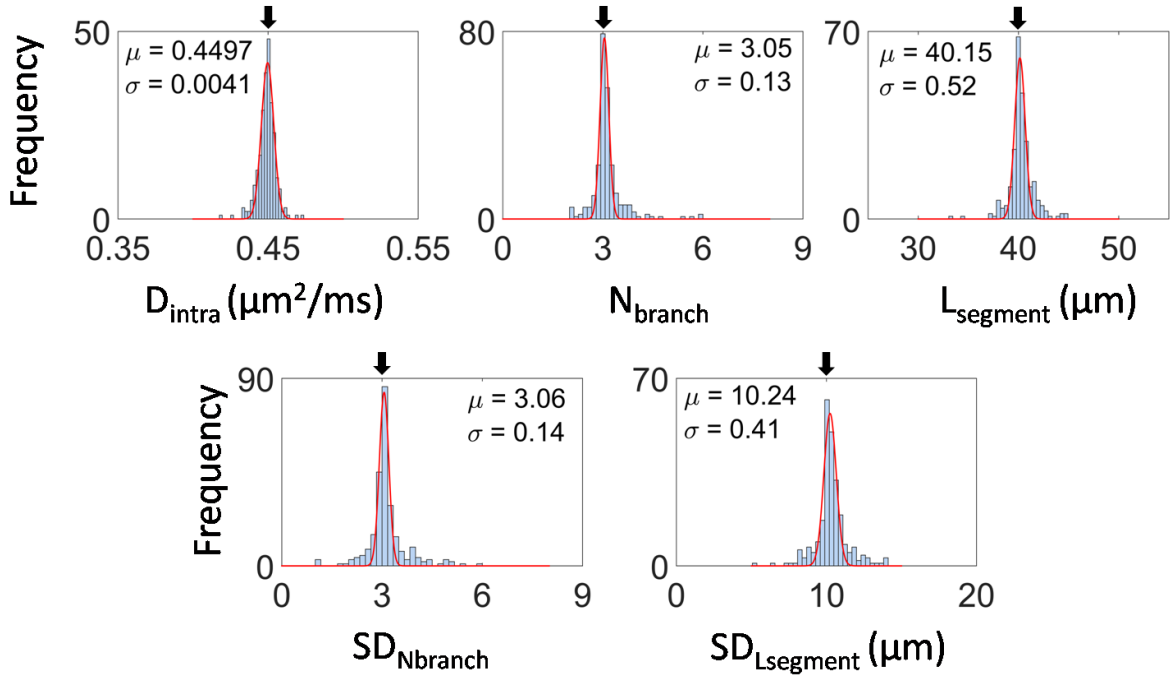

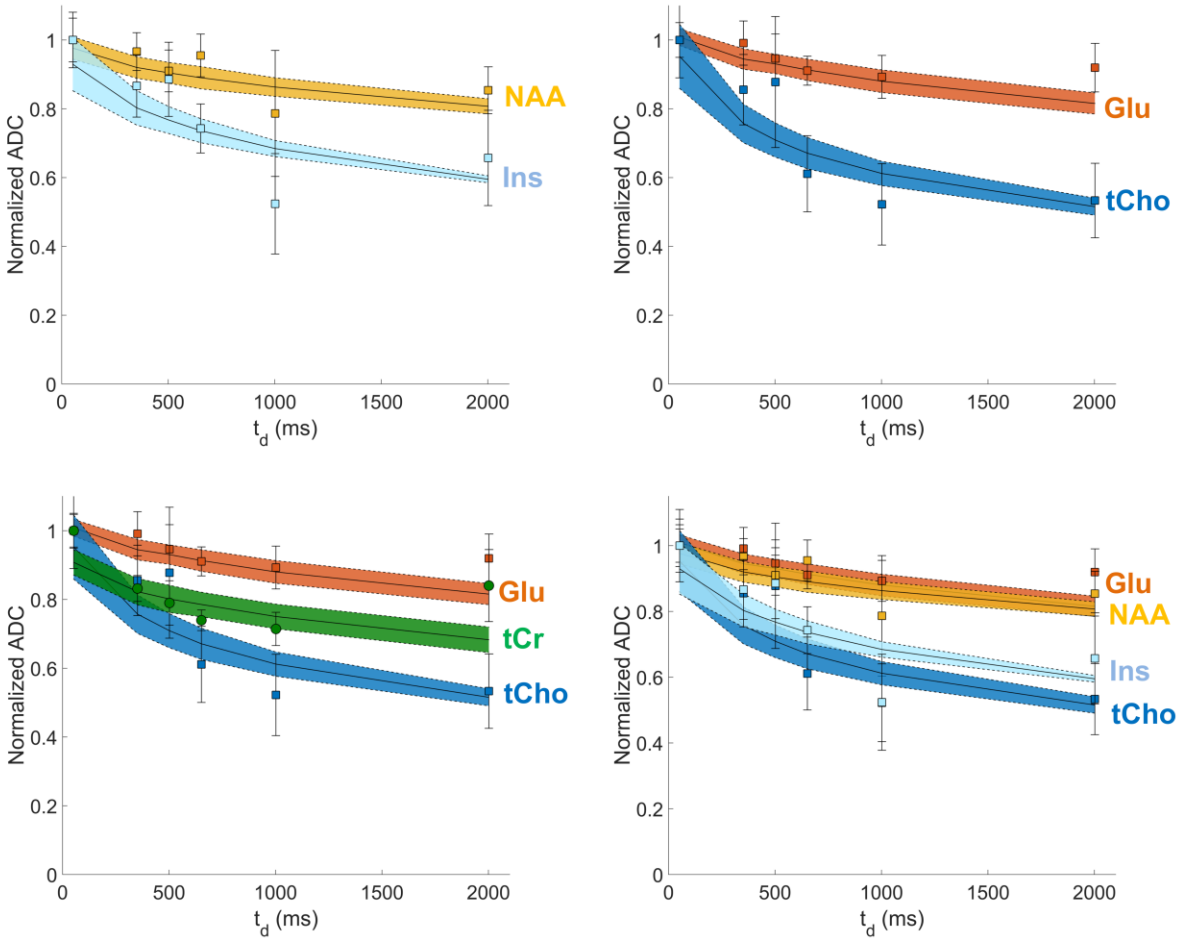

Figure S4: Illustration of metabolite diffusion behavior and fit dispersion in the mouse brain. Various comparisons of metabolite datasets are given, as well as best fits (black solid curves) and the envelopes of all fits obtained from Monte Carlo simulation of noised datasets (colored regions) (*Section VI*). For visualization purpose, data and fits are normalized relative to the data point at the shortest diffusion time. The figure is organized to facilitate comparison between metabolites thought to be preferentially neuronal (NAA and Glu) or astrocytic (Ins and tCho). The separation between "neuronal" and "astrocytic" metabolites is striking. Meanwhile, Glu and NAA overlap, and Ins and tCho also display very similar diffusion trends.

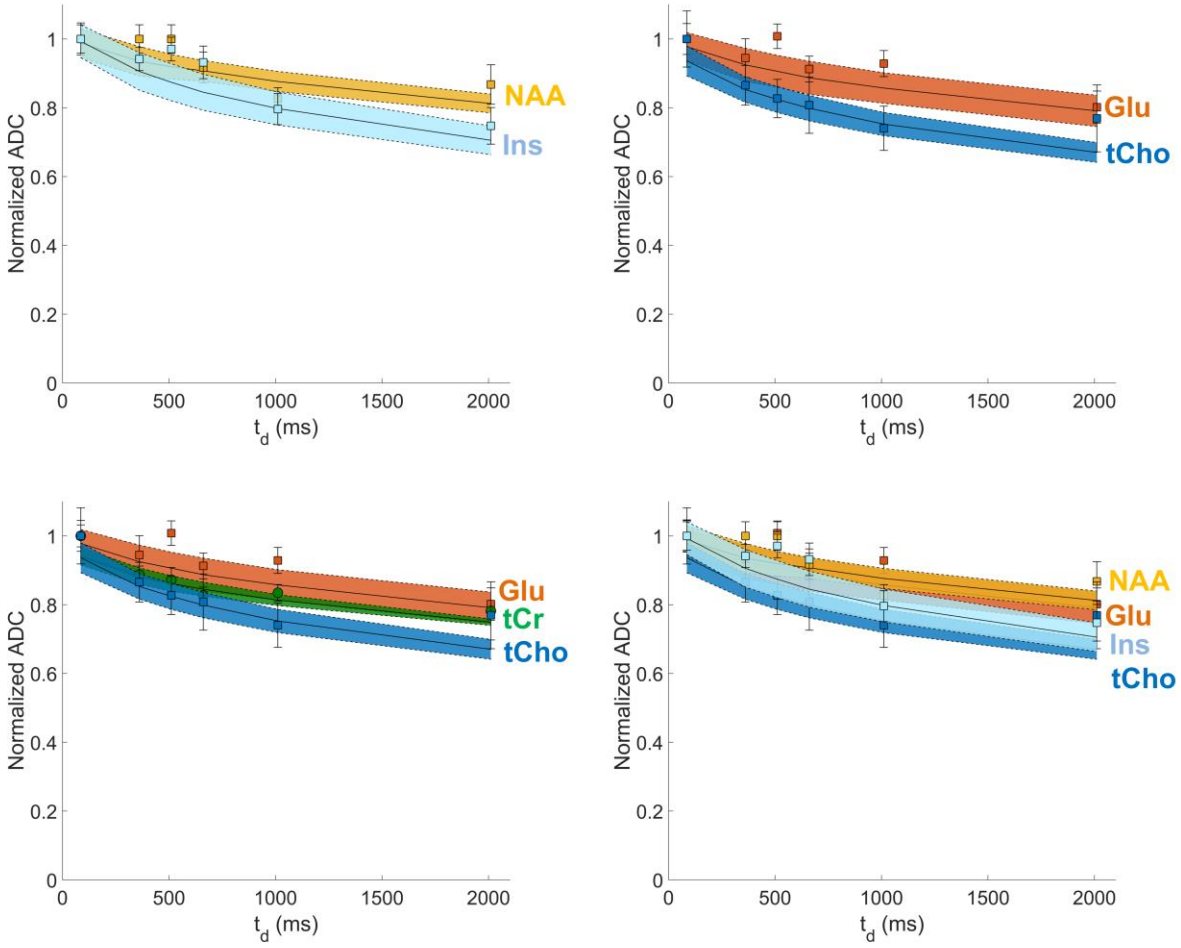

Figure S5: Illustration of metabolite diffusion behavior and fit dispersion in the monkey brain. Various comparisons of metabolite datasets are given, as well as best fits (black solid curves) and the envelopes of all fits obtained from Monte Carlo simulation of noised datasets (colored regions) (*Section VI*). For visualization purpose, data and fits are normalized relative to the data point at the shortest diffusion time. The figure is organized to facilitate comparison between metabolites thought to be preferentially neuronal (NAA and Glu) or astrocytic (Ins and tCho). The separation between "neuronal" and "astrocytic" metabolites is still visible on data and best fits, although less marked than for mice (which we interpret as astrocytes being almost as large and complex as neurons in the primate brain).

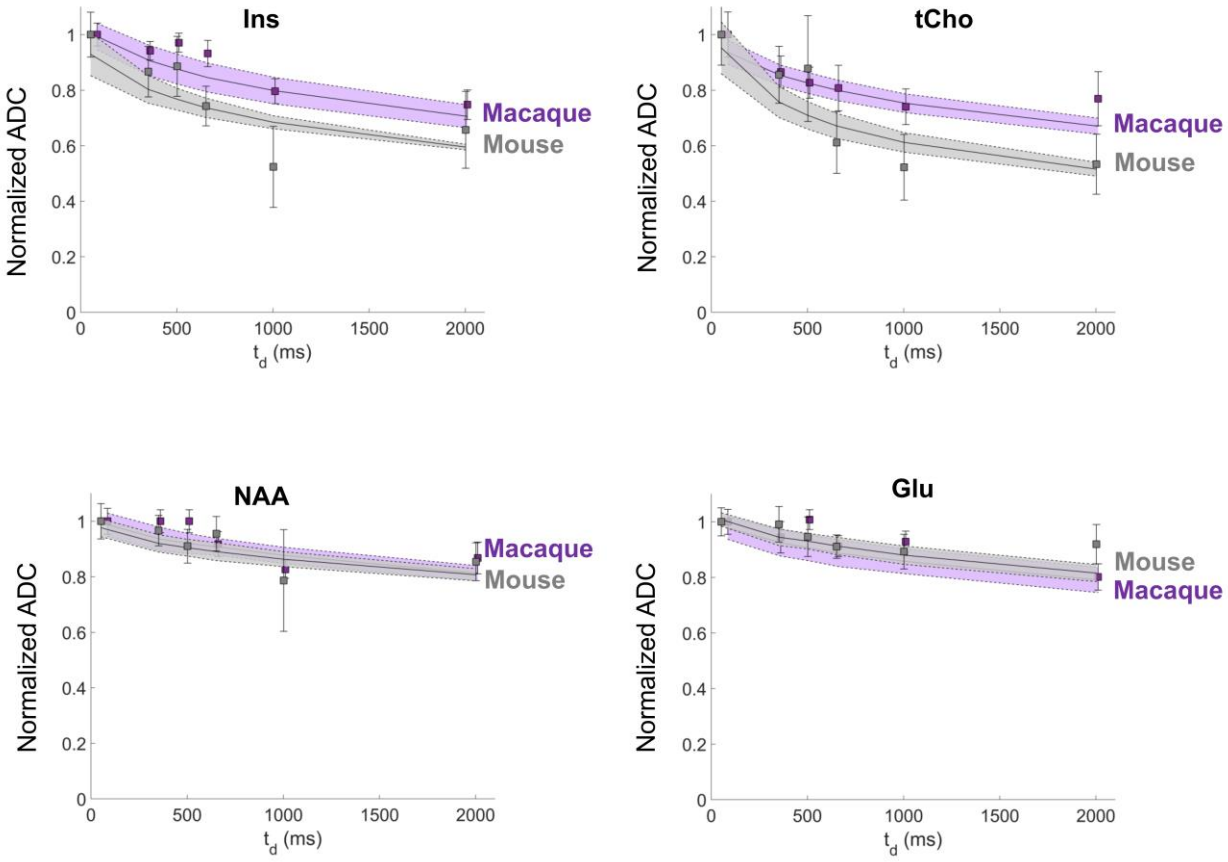

Figure S6: Illustration of metabolite diffusion behavior and fit dispersion in mouse *versus* monkey brains. Comparisons of datasets for metabolites thought to be preferentially neuronal (NAA and Glu) or astrocytic (Ins and tCho), as well as best fits (black solid curves) and envelopes of all fits obtained from Monte Carlo simulation of noised datasets (colored regions) (*Section VI*). For visualization purpose, data and fits are normalized relative to the data point at the shortest diffusion time. It appears that, while NAA and Glu have a very similar behavior, Ins and tCho have different diffusion properties between both species. This is interpreted as neurons having approximately the same morphology in both species, but astrocytes being larger/more complex in the primate brain.

Figure S7: Effect of long axons on intracellular ADC. Effect of varying the volume fraction of long axons in the synthetic tissue on the estimated parameters D_{intra} (A), $L_{segment}$ (B) and N_{branch} (C). Red solid and dashed lines represent the real mean and standard deviation values for each parameter, respectively. Error bars represent the estimated standard deviation of the corresponding parameter (i.e. $SD_{Lsegment}$ and $SD_{Nbranch}$).

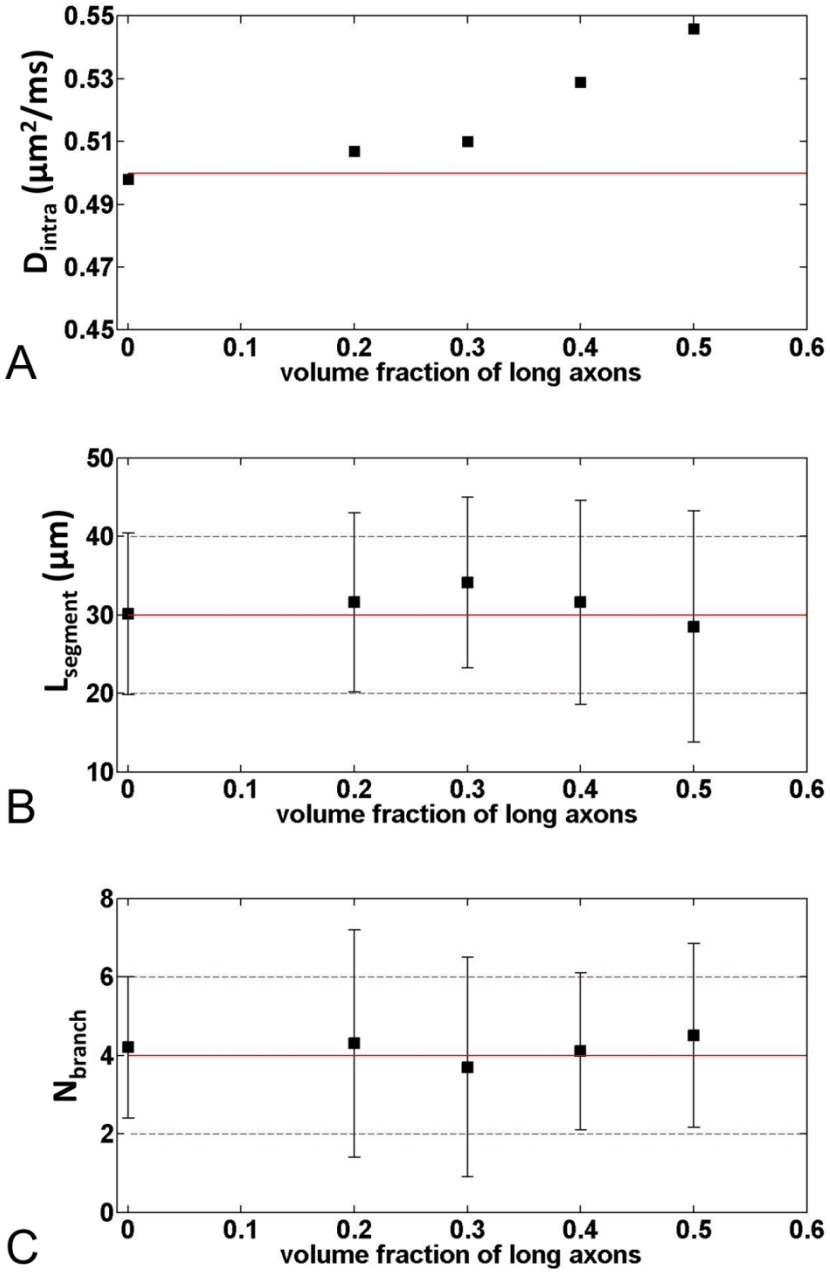

Figure S8: Three-dimensional synthetic tissues. Three-dimensional synthetic tissues obtained from the astrocytic compartments estimated by the simulation-fitting of DW-MRS data (Ins and tCho) in the mouse brain (A) and in the macaque brain (B). Grey slice represent the cut slice reported in Fig. 3 of the main text.

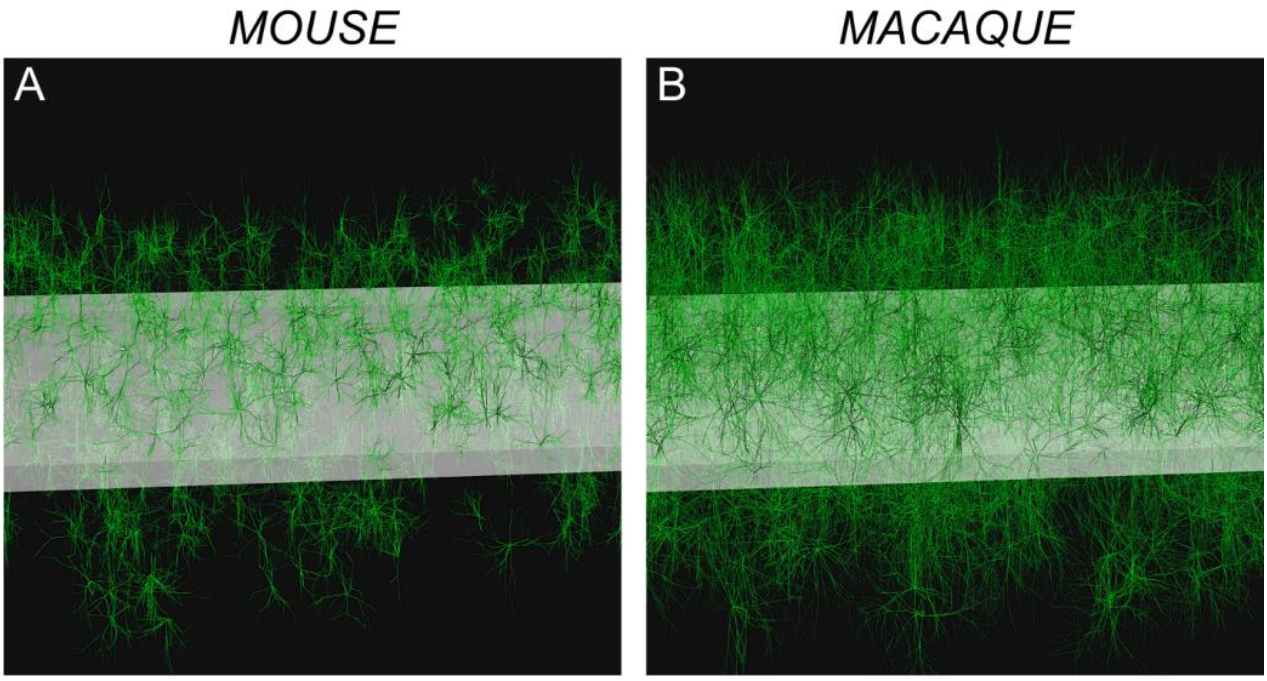

Figure S9: **Sholl analysis.** Examples of the Sholl analysis on a single astrocytic cell from a real GFAP stained slice of mouse brain and a virtually reproduced one are reported in A and B respectively. Starting from right to left, each cell is isolated within the investigated real (A) and synthetic (B) histological slice; its center is identified; and the Sholl analysis, based on statistics from concentric circles (drawn in different colors), is performed. (C) Sholl analysis results from 135 different cells were taken into account to estimate the mean and s.d. of Sholl-based metrics (see Table 2 of the main text) and here reported as histograms. No statistically significant differences were found between the Sholl-based metrics measured from real and virtual histological slices. Enclosing radius and Critical radius are given in μm.

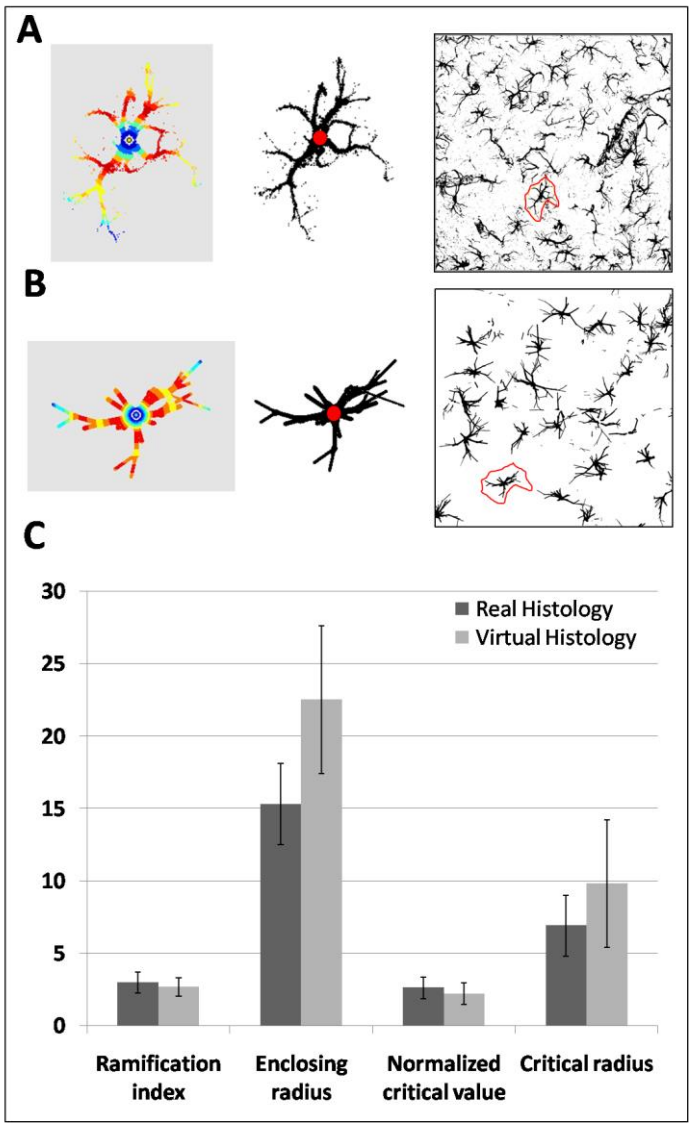

Table S1: **Metabolite ADC values estimated from DW-MRS spectra at each investigated diffusion time t_d, in the mouse and in the macaque brain.** The errors stand for the standard errors of the mean.

Metabolite	**ADC (µm^2/ms)**					
Mouse						
	t_d =52 ms	**t_d = 352 ms**	**t_d = 502 ms**	**t_d = 652 ms**	**t_d = 1002 ms**	**t_d = 2002 ms**
Ins	0.105 ± 0.006	0.091 ± 0.008	0.093 ± 0.010	0.078 ± 0.006	0.055 ± 0.015	0.069 ± 0.014
tCho	0.090 ±0.007	0.077 ± 0.007	0.079 ± 0.016	0.055 ± 0.009	0.047 ± 0.010	0.048 ± 0.009
tCr	0.119 ± 0.004	0.099 ± 0.003	0.094 ± 0.007	0.088 ± 0.002	0.085 ± 0.005	0.100 ± 0.012
Tau	0.124 ± 0.004	0.123 ± 0.005	0.091 ± 0.016	0.106 ± 0.002	0.084 ± 0.009	0.098 ± 0.006
NAA	0.089 ± 0.004	0.086 ± 0.003	0.081 ± 0.004	0.085 ± 0.004	0.070 ± 0.016	0.076 ± 0.005
Glu	0.112 ± 0.004	0.111 ± 0.006	0.106 ± 0.007	0.102 ± 0.003	0.100 ± 0.006	0.103 ± 0.007
Macaque						
	t_d =86 ms	**t_d = 361 ms**	**t_d = 511 ms**	**t_d = 661 ms**	**t_d = 1011 ms**	**t_d = 2011 ms**
Ins	0.103 ± 0.003	0.097 ± 0.002	0.100 ± 0.002	0.096 ± 0.004	0.082 ± 0.004	0.077 ± 0.005
tCho	0.104 ± 0.006	0.090 ± 0.003	0.086 ± 0.003	0.084 ± 0.007	0.077 ± 0.005	0.080 ± 0.009
tCr	0.133 ± 0.003	0.118 ± 0.002	0.116 ± 0.004	0.110 ± 0.002	0.111 ± 0.002	0.104 ± 0.011
NAA	0.121 ± 0.004	0.121 ± 0.003	0.121 ± 0.003	0.111 ± 0.004	0.100 ± 0.002	0.105 ± 0.006
Glu	0.126 ± 0.004	0.119 ± 0.006	0.127 ± 0.002	0.115 ± 0.003	0.117 ± 0.003	0.101 ± 0.005

Table S2: **Results of fitting stability analysis.** Accuracy and precision of each estimated parameters with respect to experimental noise, investigated by computing the bias and the coefficient of variation (CV) by the Monte Carlo approach described in this appendix (*Section V*).

Fitting stability to noise	D_{intra}	N_{branch}	$L_{segment}$	$SD_{Nbranch}$	$SD_{Lsegment}$
Bias (%)	-0.46	1.7	0.38	2.0	2.4
CV (%)	0.91	4.3	1.3	4.7	4.1

Table S3: **Statistical significances for inter-metabolites comparisons in the mouse brain.** The permutation test procedure used to calculate p-values is described in *Section VI*. To take into account multiple comparisons, the significant threshold was set to $p=5\times10^{-4}$. Significant differences are marked by an asterisk and are in bold.

N_{branch}

	Ins	tCho	tCr	NAA	Glu
Ins	1				
tCho	**3×10^{-4} ***	1			
tCr	0.3	**3×10^{-4} ***	1		
NAA	**5×10^{-4} ***	**5×10^{-4} ***	**2×10^{-4} ***	1	
Glu	**2×10^{-4} ***	**2×10^{-4} ***	**2×10^{-4} ***	**3×10^{-4} ***	1

$L_{segment}$

	Ins	tCho	tCr	NAA	Glu
Ins	1				
tCho	**2×10^{-4} ***	1			
tCr	**2×10^{-4} ***	**3×10^{-4} ***	1		
NAA	**3×10^{-4} ***	**2×10^{-4} ***	**3×10^{-4} ***	1	
Glu	**3×10^{-4} ***	**3×10^{-4} ***	**2×10^{-4} ***	0.3	1

$SD_{Nbranch}$

	Ins	tCho	tCr	NAA	Glu
Ins	1				
tCho	0.01	1			
tCr	3×10^{-3}	8×10^{-4}	1		
NAA	0.1	3×10^{-3}	0.01	1	
Glu	0.01	2×10^{-3}	0.2	0.07	1

$SD_{Lsegment}$

	Ins	tCho	tCr	NAA	Glu
Ins	1				
tCho	0.06	1			
tCr	0.1	0.2	1		
NAA	0.2	0.02	0.4	1	
Glu	0.09	**3×10^{-4} ***	0.2	0.04	1

Table S4: **Statistical significances for inter-metabolites comparisons in the monkey brain.** The permutation test procedure used to calculate p-values is described in *Section VI*. To take into account multiple comparisons, the significant threshold was set to $p=5\times10^{-4}$. Significant differences are marked by an asterisk and are in bold.

N_{branch}

	Ins	tCho	tCr	NAA	Glu
Ins	1				
tCho	0.2	1			
tCr	0.07	0.08	1		
NAA	1×10^{-3}	9×10^{-4}	0.1	1	
Glu	0.04	0.01	0.1	0.1	1

$L_{segment}$

	Ins	tCho	tCr	NAA	Glu
Ins	1				
tCho	**4×10^{-4} ***	1			
tCr	**4×10^{-4} ***	**4×10^{-4} ***	1		
NAA	**3×10^{-4} ***	**3×10^{-4} ***	0.05	1	
Glu	**3×10^{-4} ***	**2×10^{-4} ***	0.03	**5×10^{-4} ***	1

$SD_{Nbranch}$

	Ins	tCho	tCr	NAA	Glu
Ins	1				
tCho	0.6	1			
tCr	0.7	0.6	1		
NAA	0.04	0.03	0.02	1	
Glu	0.9	0.7	0.8	0.02	1

$SD_{Lsegment}$

	Ins	tCho	tCr	NAA	Glu
Ins	1				
tCho	0.08	1			
tCr	0.3	0.5	1		
NAA	**1×10^{-4} ***	0.04	0.3	1	
Glu	**4×10^{-4} ***	0.03	0.3	**3×10^{-4} ***	1

Table S5: **Statistical significances for interspecies comparisons.** The permutation test procedure used to calculate p-values is described in *Section VI*. To take into account multiple comparisons, the significant threshold was set to $p=5\times10^{-4}$. Significant differences are marked by an asterisk and are in bold.

	N_{branch}	$L_{segment}$	$SD_{Nbranch}$	$SD_{Lsegment}$
Ins	**2×10^{-4} ***	**3×10^{-4} ***	0.09	**4×10^{-4} ***
tCho	**3×10^{-4} ***	**2×10^{-4} ***	0.2	**4×10^{-4} ***
tCr	**3×10^{-4} ***	**4×10^{-4} ***	0.4	0.1
NAA	**5×10^{-4} ***	7×10^{-4}	0.09	**4×10^{-4} ***
Glu	0.5	0.3	0.2	0.03